Dissolution reaction and surface iron speciation of UICC crocidolite in buffered solution at pH 7.4: A combined ICP-OES, XPS and TEM investigation

(Article begins on next page)

20 April 2024

UNIVERSITÀ DEGLI STUDI DI TORINO

1   **Revision 1**

2   Dissolution reaction and surface iron speciation of UICC crocidolite

3   in buffered solution at pH 7.4: a combined ICP-OES, XPS and TEM

4   investigation

5

6   Alessandro Pacella[1], Marzia Fantauzzi[2], FrancescoTurci[3,4], Carlo Cremisini[5], Maria Rita

7   Montereali[5], Elisa Nardi[5], Davide Atzei[2], Antonella Rossi[2,*], and Giovanni B. Andreozzi[1,6,*]

8

9   [1]Dipartimento di Scienze della Terra, Sapienza Università di Roma, Piazzale Aldo Moro 5, I-

10   00185 Roma, Italy

11   [2]Dipartimento di Scienze Chimiche e Geologiche, INSTM research unit, Centro Grandi

12   Strumenti Università di Cagliari, I-09042 Monserrato, Cagliari, Italy

13   [3]'G. Scansetti' Interdepartmental Centre for Studies on Asbestos and Other Toxic

14   Particulates, Università di Torino, via Pietro Giuria 9, I-10125 Torino, Italy

15   [4]Dipartimento di Chimica, Università di Torino, via Pietro Giuria 7, I-10125 Torino, Italy

16   [5]ENEA, C.R. Casaccia via Anguillarese 301, I-00123 S. Maria di Galeria, Roma, Italy

17   [6] CNR-IGG, U.O. Roma, c/o Dipartimento di Scienze della Terra, Sapienza Università di

18   Roma, Piazzale Aldo Moro 5, I-00185 Roma, Italy

19

20   *CorrespondingAuthors:

21

22   Prof. Giovanni B. Andreozzi

23   Dipartimento di Scienze della Terra, Sapienza Università di Roma, Piazzale Aldo Moro 5, I-

24   00185 Roma, Italy

25   e-mail: gianni.andreozzi@uniroma1.it

26

27   Prof. Antonella Rossi

28   Dipartimento di Scienze Chimiche e Geologiche, INSTM research unit, Centro Grandi

29   Strumenti, Università di Cagliari, I-09042 Monserrato, Cagliari, Italy

30   Phone: +39 070 6754464 - Fax: +39 070 6754459

31   e-mail: rossi@unica.it

32

33 **Abstract**

34 The dissolution reaction and the surface modifications of crocidolite asbestos fibres incubated

35 for 0.5, 1, 24, 48, 168 and 1440 h in a phosphate buffered solution at pH 7.4 with and without

36 hydrogen peroxide were investigated. Inductively Coupled Plasma Optical Emission

37 Spectrometry (ICP-OES) was used to monitor the ion release into solution, X-Ray

38 Photoelectron Spectroscopy (XPS) was performed to unveil the chemistry of the leached

39 surface, and High Resolution Transmission Electron Microscopy (HR-TEM) was carried out

40 to monitor the structural modifications of the fibres. No significant differences were observed

41 between dissolution experiments carried out with and without H_2O_2 with the exception of

42 results after the first hour, from which it may be inferred that the dissolution proceeds faster

43 in the presence of H_2O_2 but only in its very early steps. Congruent mobilization of Si and Mg

44 from crocidolite was observed, increasing with time especially in the range between 1 and 48

45 h, while Ca decreased after 48 h and Fe was not detected at any incubation time. In the under-

46 saturated conditions (0-48 h), dissolution rate of UICC crocidolite fibres has been estimated to

47 be $d(Si)/dt = 0.079$ μmol h^{-1}. The fibre surface modification is continuous with time: XPS

48 results showed a regular depletion of Si and Mg and enrichment of Fe along dissolution. The

49 $Fe2p_{3/2}$ signal on the surface was fitted with four components at 709.0, 710.5, 711.6 and 712.8

50 eV binding energy values corresponding to: i) Fe(II)-O and ii) Fe(III)-O surrounded by

51 oxygen atoms in the silicate structure, iii) Fe(III)-OOH as a product of the dissolution process,

52 and iv) Fe in a phosphate precipitate (Fe-P), respectively. The evolution of Fe speciation on

53 the crocidolite surface was followed by integrating the four photoemission peaks, and results

54 showed that the oxidative environment promotes the formation of Fe(III)-O (up to 37% Fe_{tot})

55 and of Fe-P species (up to 16% Fe_{tot}), which are found on the fibre surface at the end of the

56 dissolution experiment. HR-TEM showed that the crocidolite lattice structure, the fibrous

57 habit and the high aspect ratio are preserved upon leaching, while Fe-bearing nanoparticles,

58 likely amorphous and possibly displaced on top of the fibres, become clearly visible. As a

59 conclusion, coating of the crocidolite fibres was demonstrated to occur due to precipitation of

60 Fe-rich phases (both phosphates and oxide-hydroxides). The occurrence of such iron

61 armouring may modulate asbestos toxicity and possibly be the initial step in the formation of

62 asbestos ferruginous bodies.

63

66

1. INTRODUCTION

67
68

69 Asbestos materials are made of six hydrate silicate minerals with fibrous morphology:

70 chrysotile, the only fibrous member of the serpentine mineral group, with ideal chemical

71 formula $Mg_3Si_2O_5(OH)_4$; anthophyllite, belonging to the amphibole supergroup, ideally

72 $Mg_7Si_8O_{22}(OH)_2$; grunerite amphibole, ideally $Fe^{2+}_7Si_8O_{22}(OH)_2$, usually referred to

73 colloquially as "amosite" (from the acronym AMOS, Asbestos Mines of South Africa);

74 tremolite amphibole, ideally $Ca_2Mg_5Si_8O_{22}(OH)_2$; ferro-actinolite amphibole, ideally

75 $Ca_2Fe^{2+}_5Si_8O_{22}(OH)_2$; riebeckite amphibole, ideally $Na_2(Fe^{2+}_3Fe^{3+}_2)_{\Sigma=5}Si_8O_{22}(OH)_2$, usually

76 referred to colloquially as "crocidolite" (from the Greek κροκύς, nap of cloth, on account of

77 its nap-like appearance).

78 Innumerable epidemiological studies have shown that exposure to asbestos is related to

79 several health problems and respiratory diseases. The molecular basis of asbestos-induced

80 lung disease has not been fully elucidated yet (Liu et al., 2013; Pascolo et al., 2013).

81 However, it is widely held (e.g., Stanton et al., 1981; Kamp and Weitzman, 1999) that size –

82 in particular the aspect ratio–, surface reactivity, and biopersistence are the three main factors

83 in determining the pathological response to asbestos. This paradigm holds for many

84 hazardous inhaled particles and fibres (Hochella, 1993; Fubini et al., 1995; Fubini, 1997;

85 Hohr et al., 2002; Fubini et al., 2011). The most robust mechanism-based structure-activity

86 relationship for asbestos includes generation of iron-mediated reactive oxygen species (ROS)

87 (Fubini and Otero-Areàn, 1999; Shukla et al., 2003). Such chemical activity received

88 considerable attention by the biomedical community and was related to the presence and the

89 bioavailability of Fe. Both the presence and the structural coordination of Fe were showed to

90 be important factors of asbestos toxicity (Turci et al., 2011). Tests performed on isolated

91 mitochondria in contact with iron-rich crocidolite showed that crocidolite causes severe

92 damage to cells and enhances the mitochondrial production of ROS (Bergamini et al., 2007).

93 Furthermore, only the Fe on the fibre surface, and in particular Fe(II), was considered to play

94 a primary role for the ROS production (Hardy and Aust, 1995; Pacella et al., 2010, 2012;

95 Fantauzzi et al., 2010; 2012).The increase in the surface concentration of Fe on asbestos

96 fibres upon treatment with murine tumor cells and culture medium was reported by Seal et al.

97 (1996, 1997). However, no attempts of quantification of Fe(II) and Fe(III) speciation were

98 done by the authors. Studies on crocidolite dissolution in the presence of Fe chelators showed

99 that the presence of chelators dramatically increases Fe(III) release, with Fe-release lifetime

100 estimated to be on the order of 10 years (Werner et al., 1995). It was reported that Fe can be

101 mobilized from crocidolite in lung cells with a rate similar to that observed in vitro when
102 crocidolite was incubated with citrate, enhancing asbestos ability to catalyse damages to DNA
103 (Lund and Aust, 1992; Chao et al., 1994). Endogenous chelators present in the lung lining
104 layer fluid, such as ascorbic acid, were shown to be responsible for an effective iron
105 mobilization from crocidolite fibres (Martra et al., 2003). It was also demonstrated by in vitro
106 studies that ferruginous bodies, mainly constituted by ferrihydrite, might precipitate on
107 asbestos fibres in contact with human cells (Shen et al., 2000). In addition, precipitation of
108 calcium phosphates was observed upon interaction between chrysotile asbestos and simulated
109 lung fluids, and SEM analyses of calcified pleural plaques detected the presence of
110 hydroxyapatite secondary phases in lung tissues (Taunton et al., 2010).

111 The aim of the present work is describing the dissolution dynamics and the surface
112 modifications of crocidolite asbestos incubated at 37 °C in a hydrogen peroxide solution
113 buffered at pH = 7.4. The extreme incubation conditions used are based on the approach
114 previously adopted by some of us for measuring the surface reactivity of the UICC crocidolite
115 (Pacella et al., 2012). Even being far from mimic a real cellular environment, such conditions
116 were chosen to promote the dissolution dynamics that may occur in vivo in a reasonable
117 experimental time. A sample of reference crocidolite, supplied by the Union Internationale
118 Contre le Cancer (UICC), hereafter named UICC crocidolite, was suspended in the leaching
119 solution from 0.5 h to 1440 h (two months) and then investigated by a multi-analytical
120 approach. Ion release was monitored by Inductively Coupled Plasma Optical Emission
121 Spectrometry (ICP-OES). Modification of surface chemistry, including Fe(II) and Fe(III)
122 speciation, was investigated by X-ray Photoelectron Spectroscopy (XPS); structural state of
123 the fibres before and after dissolution experiments was studied by High Resolution
124 Transmission Electron Microscopy (HR-TEM).

125

126   **2. EXPERIMENTAL**

127

128   **2.1.Materials**

129

130 The sample investigated consists of fibres of UICC crocidolite selected under microscope and
131 gently ground for 1 min under acetone in an agate mortar. Chemical formula is
132 $[(K_{0.01}Na_{1.64}Ca_{0.14}Mg_{0.16})_{\Sigma=1.95}(Fe^{2+}_{2.13}Fe^{3+}_{2.30}Mg_{0.55}Mn_{0.01}Ti_{0.01})_{\Sigma=5.00}(Si_{7.82}Al_{0.02})_{\Sigma=7.84}O_{22}(OH)$
133 $_{2.1}]$, fairly close to that of the ideal crocidolite $Na_2(Fe^{2+}_3Fe^{3+}_2)_{\Sigma=5}Si_8O_{22}(OH)_2$. The

134 morphology of the fibres was investigated by Field-Emission Scanning Electron Microscopy

135 (FE-SEM), and surface area was measured by nitrogen physisorption (BET).

136

137   **2.2. Dissolution experiments**

138

139 For the preparation of the leaching solution "ultrapure" deionised water (18.2 $M\Omega$ cm at

140 25°C) obtained from a MilliQ Element system (Millipore, France) and the following reagents

141 and materials were used: potassium dihydrogen phosphate (KH_2PO_4 - RPE - Carlo Erba

142 Reagenti, Italy), 30% hydrogen peroxide (H_2O_2 - "suprapure" - Merck, Germany);

143 Polypropylene Falcon Tubes (Blue Max)^{TM}, syringes BD Plastipack^{TM} and 0.22 μm GSWP

144 nitrocellulose membrane filters (Millex HA, Millipore).

145 An amount of 68.0 g of KH_2PO_4 was dissolved in "ultrapure" water in a 1 dm^3 volumetric

146 flask; 10 cm^3 of 30% H_2O_2 were added (to obtain a concentration of 0.3% in the 1 dm^3 final

147 volume of the solution); pH was adjusted to 7.4 with a 1N potassium hydroxide solution

148 (Normex - Carlo Erba Reagenti, Italy) and finally "ultrapure" water was added up to the final

149 1 dm^3 volume. The experimental conditions used here are based on the approach described by

150 Nejjari et al. (1993) and adopted by Pacella et al.(2012) for measuring surface reactivity of the

151 UICC crocidolite.

152 For the dissolution experiments an amount of 25 mg of fibres of UICC crocidolite, placed in a

153 Falcon^{TM} polypropylene tube, was suspended in 2 cm^3 of the potassium phosphate/hydrogen

154 peroxide buffer solution above described. The tube was continuously shaken in a thermostatic

155 oscillating bath at 37°C. Independent experiments were conducted for 0.5, 1, 24, 48, 168

156 hours (1 week) and 1440 hours (2 months). For each single experiment leaching tests were

157 performed in triplicate and a blank procedure was always carried out. In addition, the UICC

158 crocidolite fibres were also tested in the potassium phosphate buffer solution at pH 7.4

159 prepared without H_2O_2, in order to evaluate the effect of the oxidizing ambient on the cation

160 dissolution.

161 For each experiment the solution was sampled with a syringe from the tube, after

162 centrifugation at 3000 revolution per minute (rpm) for 5 min, and filtered in nitrocellulose

163 membrane filter of 0.22 μm. From each filtered solution 1 cm^3 diluted 1:20 with a 1% nitric

164 acid solution was analysed by ICP-OES (see paragraph 2.3).

165   The fibres were recovered from the tubes on filters, rinsed with ultrapure deionised water to

166   eliminate the residues of the solution, dried and then stored under argon prior to the XPS

167   measurements.

168

169   **2.3.ICP-OES investigation**

170

171   One cm^3 of each filtered solution was diluted (1:20) with a 1% nitric acid solution and

172   analyzed by ICP-OES in order to measure the concentration of leached Si, Mg, Ca and Fe

173   from the fibers. All measurements were performed using a Perkin Elmer Optima 2000 DV

174   ICP-OES spectrometer (Perkin Elmer, USA) equipped with a cross flow nebulizer placed

175   inside a Scott spray chamber. ICP Aristar (BDH) standard solutions in nitric acid for Si

176   (10.000 mg dm^{-3}), Mg, Ca, Fe (1000 mg dm^{-3}) were used to prepare the calibrating solutions

177   for ICP-OES analyses. The standard solutions used for the calibrations were prepared as the

178   samples using potassium phosphate buffer solution, with 0.3 % H_2O_2 (or, in case, without),

179   diluted 1:20 with a 1% nitric acid solution. To ensure adequate quality assurance, the

180   measures of the standard solutions were regularly repeated after the measurements of each

181   single experiment. Data reported are the mean values of triplicate measurements (corrected

182   considering data from the blank procedure).

183

184   **2.4.XPS investigation**

185

186   XPS analyses were performed on a Theta Probe (Thermo Fisher Scientific, Waltham MA,

187   USA). Fibrous samples were deposited on polycarbonate filters (0.4 μm) and mounted on a

188   standard sample holder for XPS measurements with copper clips. Spectra were collected

189   using a monochromatic source (Al $k\alpha_{1,2}$ energy = 1486.6 eV). The spot size was 300 μm and

190   the beam was operated at 4.7 mA and 15 kV (70 W). The residual pressure into the main

191   chamber was lower than 10^{-7} Pa. The instrument is also equipped with a neutralizer for charge

192   compensation. Survey spectra were acquired in fixed analyser transmission mode (FAT) using

193   a pass energy (PE) of 200 eV, while the high-resolution spectra of C1s, O1s, Si2p, Mg1s,

194   Ca2p, Na1s, K2p, Fe2p and P2p were collected with a PE of 100 eV selecting the standard

195   lens mode; the full-width at half-maximum of the peak height, FWHM, of the silver $Ag3d_{5/2}$

196   signal for the high-resolution spectra was 0.83 eV; step size of 1 eV and 0.05 eV were set

197   respectively. The emission angle is of 53°, and the angle between the source and the analyser

198   axis is 63.78°. To verify the linear response of the instrument, periodic calibrations were

199 performed according to ISO 2001. When analysing the fibres the neutralizer was used to
200 compensate for sample charging and the binding energy values were further corrected with
201 reference to the adventitious aliphatic carbon at 285.0 eV. Data were acquired under computer
202 control (Avantage v 3.45). Three different areas were analysed on each sample.

203 To determine the peak areas and the elemental composition, the spectra were processed using
204 CASAXPS software (Fairley, 1999-2003). Before applying the curve-fitting procedure, the
205 background was subtracted according to the Shirley-Sherwood background subtraction
206 method (Shirley, 1972). The product of Gaussian and Lorentzian functions was used for curve
207 fitting. Quantitative analysis of fibre surfaces was performed using the first-principle method
208 (Seah, 2003) on the assumption that the sample was homogeneous. Peak areas were corrected
209 for the sensitivity factors calculated using Scofield's photoionization cross-sections σ
210 (Scofield, 1976); the asymmetry parameters (Reilman et al., 1976), the inelastic mean free
211 paths (IMFP) and the intensity/energy analyser response were determined according to the
212 procedure provided in Avantage Software v. 3.45. IMFP were calculated according to Gries
213 (1996). The accuracy of the calculated atomic concentrations is estimated to be $\pm$ 10%.
214 Binding energy values and atomic percentages are reported in this work as means on at least
215 three independent measurements with their corresponding standard deviations.

216

217   **2.5.HR-TEM investigation**

218

219 The morphology and crystalline structure of the samples before and after dissolution
220 experiments were investigated by JEOL 3010-UHR HR-TEM equipped with a LaB_6 filament
221 operated at 300 kV, beam current 114 μA and equipped with a 2k x 2k pixels Gatan US1000
222 CCD camera. Elemental analysis was performed by Oxford INCA X-ray energy dispersive
223 spectrometer (X-EDS) with a Pentafet Si(Li) detector. Crocidolite fibres were dispersed in
224 ultrapure water (MilliQ system, Millipore), sonicated for 20 minutes and a droplet was
225 deposited on lacey carbon Cu grids.

226

227   **3. RESULTS**

228

229 The UICC crocidolite fibres appear straight, rigid and very tiny under binocular microscope.
230 FE-SEM images show that most of the fibres have a polygonal cross section with major
231 diameter in the range of 0.5-1 μm. Notably, high resolution images show that the micrometric
232 fibres have the possibility of parting into fibrils with diameter of ca. 0.1 μm (**Fig. 1**).

233   Results of ICP-OES analyses after suspension experiments in the phosphate buffer solution

234   with H_2O_2 reveal that some dissolution occurred from early steps, as evidenced by the release

235   of Si, Mg and Ca (**Table 1**). In particular, Si release ranges from 624 mg/kg after 0.5 h to

236   5120 mg/kg after two months of dissolution time, and Mg ranges from 180 mg/kg to 590

237   mg/kg in the same period of time. Calcium release equals 877 mg/kg after 0.5 h, reaches a

238   maximum about 1500 mg/kg after 24-48 h and then markedly decreases down to 866 mg/kg.

239   The analysis of the progression of cation dissolution reveals the existence of two regions: 1)

240   between zero and 48h, representing the under-saturation conditions, favourable to fibre

241   solubility; 2) after 48h –and markedly after 168h– representing the near-saturation conditions,

242   where element release is very low or below the detection limit (**Fig. 2**). In particular, Ca

243   release is observed to slow down after 24 h experiment, and to stop after 48 h, suggesting a

244   possible Ca precipitation. Notably, mobilization of Fe was not observed for any dissolution

245   time, even extending the experiments up to two months. For the experimental conditions

246   adopted here the detection limit for Fe was 50 $\mu g\ dm^{-3}$, approximately corresponding to a

247   leaching of less than 0.03% of the total Fe content in the crocidolite sample.

248   The dissolution experiments were repeated from 1 to 168 hours without H_2O_2: results of ICP-

249   OES analyses did not show marked differences with the exception of results after the first

250   hour of incubation (**Table 1**), from which it may be inferred that the dissolution proceeds

251   faster in the presence of H_2O_2 but only in its very early steps. In both conditions Si and Mg

252   are released congruently, that is in a proportion roughly corresponding to crocidolite bulk and

253   surface stoichiometry (**Fig. 3**), in agreement with results obtained by Gronow (1987). On the

254   contrary, Ca release is definitely in excess, being the maximum value in solution three times

255   that of Mg (whereas in the crystal chemical formula of the UICC crocidolite Ca is one fifth of

256   Mg). This may be due to Ca-bearing accessory phases present in the sample but not detectable

257   in sample characterization.

258   Kinetics of the UICC crocidolite dissolution are described on the basis of ICP results. During

259   silicate dissolution it is well known that the Si release is the rate-limiting step controlling

260   dissolution rates (Oze and Solt, 2010, and references therein). In our case, Si release reaches a

261   close-to-saturation condition after 168h, with Si in the solution corresponding to less than 2%

262   of the total Si of the suspended fibres. If steady-state conditions were maintained and the

263   observed trend was extended in time, more than 100 years would be required to release only

264   4% of Si, leading to fibre dissolution rate extremely low (or close to zero). However, it is

265   known from literature that body fluids are continually replenished and fibre dissolution rates

266 are calculated for undersaturated conditions at constant pH (Hume and Rimstidt, 1992; Oze

267 and Solt, 2010). Accordingly, for UICC crocidolite the fibre dissolution rate was quantified in

268 the undersaturated initial conditions (0-48 h). Following previous authors, the rate of asbestos

269 dissolution was modelled by the simplified equation: $d(Si)/dt = k*\{A\}^n$, where $d(Si)/dt$ is the

270 rate of Si release ($\mu mol\ h^{-1}$), k is the rate constant ($\mu mol\ m^{-2*n}\ h^{-1}$), $\{A\}$ is the total surface

271 area (in m^2), and n is the reaction order. In our case, the rate of Si release is estimated using

272 the linear regression described by the equation $d(Si)/dt = 0.079\ \mu mol\ h^{-1}$, $[R^2 = 0.77]$ and the

273 surface area was measured by BET ($8.66\ m^2\ g^{-1}$). At the moment, data available do not allow

274 the calculation of the reaction order because leaching experiments were performed without

275 using different surface areas.

276 Surface quantitative analysis of UICC crocidolite fibres treated with H_2O_2 was obtained by

277 XPS, assuming as first approximation a homogeneous composition throughout the sampling

278 depth, and results are reported in **Table 2**. The identification of the elements present on the

279 UICC crocidolite fibres was possible by the XP-survey spectra (data not shown – Figure A.1

280 in the Appendix A). The elements O, Si, Fe, Na and Mg were detected on both the untreated

281 and treated samples, whereas the photoemission signals of K, P and Ca only appeared on

282 treated fibres. In particular, the Ca signal appeared after 24 h. **Table 2** also shows the results

283 obtained only considering Si, Ca, Mg and Fe, to be compared with the ICP-OES results.

284 Binding energy (BE) values of the curve-fitted spectra are summarized in **Table 3**. Si 2p peak

285 was resolved using the doublet $Si2p_{3/2}$ and $Si2p_{1/2}$ with an energy separation, ΔE, of 0.805 eV

286 and an area ratio of 2. The BE of the Si2p peaks (102.4 ± 0.2 eV) was not influenced by the

287 cation mobilization and it is in agreement with the BE value reported in Fantauzzi et al.

288 (2010) for untreated UICC crocidolite (corresponding to t = 0 h in **Table 3**). Mg 2p and Na1s

289 BE values were also independent from the dissolution time and are in agreement with those

290 reported in Fantauzzi et al. (2010). The BE of $Ca2p_{3/2}$ (347.8 ± 0.2 eV) is in agreement with

291 both $Ca2p_{3/2}$ in tremolite (Fantauzzi et al. 2010) and $Ca2p_{3/2}$ in $CaHPO_4$ and $CaHPO_4*2H_2O$

292 (Landis and Martin, 1984). In addition, the BE in a calcium metaphosphate glass has been

293 measured to be 347.0 eV (Mura, 2010). The observed presence of K ($K2p_{3/2} = 293.1 \pm 0.2$ eV)

294 on the fibre surfaces after incubation is due to the potassium phosphate used for buffer

295 preparation, that is very likely adsorbed onto the fibres. The same evidence was provided by

296 Gold et al. (1997). Due to adsorbed buffer on the fibre surfaces, phosphorus signals were

297 detected on the sample surfaces at 133.8 ± 0.2 eV (**Table 3**), which is the BE of phosphorus in

298 phosphates (Crobu et al., 2010 and references cited therein). It is worth noting that the P

299 content increases with the dissolution time (from 4% after 1 h to 7% after 168 h, **Table 2**).

300   Significant variations were observed for the $Fe2p_{3/2}$ spectrum when comparing data

301   previously obtained on untreated fibres (Fantauzzi et al., 2010), with those obtained in this

302   work for the fibres suspended in the buffered solution. According to Fantauzzi et al. (2010),

303   the $Fe2p_{3/2}$ curve fitting was performed using the convolution of Gaussian – Lorentzian

304   function based on a multiplet-splitting approach (**Fig.4**). The Fe peak of untreated UICC

305   crocidolite was fitted with three components at 709.0, 710.5 and 711.6 eV assigned to:1)

306   Fe(II) bonded to the O atoms in the silicates cavities [hereafter indicated as Fe(II)-O];2)

307   Fe(III) bonded to the O atoms in the silicates cavities [hereafter indicated as Fe(III)-O]; and 3)

308   Fe(III) oxide-hydroxide[hereafter indicated as Fe(III)-OOH], respectively (**Table 3**). In the

309   present case, a fourth component appeared at 712.8 eV. This component is attributable to an

310   iron phosphate phase (Rossi et al., 2006; Crobu, 2012) [hereafter indicated as Fe-P] which is

311   insoluble in neutral solutions. The intensity of the Fe(II)-O signal reaches the maximum value

312   of 29% of the total peak area after 1 h of dissolution and then keeps constant at about 25%;

313   the Fe(III)-O signal increases almost regularly with time from 18% to 37%; the Fe(III)-OOH

314   signal decreases from 62% to 20%, following a nearly exponential trend in the first 24 h and

315   then a linear trend up to 168 h; the Fe-P signal is zero at t = 0 and increases almost regularly

316   from 8% to 16% when increasing the dissolution time (**Fig. 5**). Notably, when comparing data

317   of surface composition obtained on fibres suspended in the solution with H_2O_2 with those

318   obtained on fibres suspended in the solution without H_2O_2, no significant differences were

319   observed (data not shown – Figures A.2 and A.3 in the Appendix A).

320   To further investigate the effect of the leaching solution on UICC crocidolite fibres, HR-TEM

321   images have been collected on fibres incubated in hydrogen peroxide buffered solution for

322   one week (168 h), and pristine fibre was examined for comparison. Representative low-and

323   high-resolution images are shown in **Figures 6 and 7**, respectively. The pristine sample

324   shows bundle of long and thin fibres with size and morphology comparable with previous

325   reports (see for example Gunter et al., 2007). The fibre bundle splits in several thinner fibres

326   up to structure of two/three associated single-crystal fibrils (**Fig. 6C**). High-resolution image

327   (**Fig. 6D**) clearly shows diffraction fringes arising from the well-ordered crystalline lattice of

328   the amphibole, as witnessed by the presence of lattice fringes with d_{hkl} fully compatible with

329   those of the crocidolite lattice (**Table 4**). In this respect, for instance, the spacing 4.876 Å

330   evidenced in **Figure 6D** corresponds to the (-1 1 1) lattice planes (JCPDS card no. 19-1061).

331   The dissolution experiments with H_2O_2 did not significantly alter the crocidolite even after

332   168 h: in fact, fibrous habit and high aspect ratio are indeed preserved after dissolution (**Fig.**

333   **7A**). The crystalline structure of treated crocidolite remains also largely unaltered as indicated

334   by the lattice fringes evidenced by HR-TEM (**Fig. 7D and Table 4**). This is consistent with

335   the well-known high persistence of amphibole structure. However, at higher magnifications,

336   the HR-TEM analysis shows the alteration the crocidolite underwent, because Fe-bearing

337   nanoparticles become clearly visible (**Fig. 7 B–D**). These nanoparticles are likely amorphous

338   and possibly displaced on top of the fibres, since the continuum of crocidolite fringes is

339   preserved throughout the new-formed particles.

340

341   **4. DISCUSSION**

342

343   The dissolution of UICC crocidolite leads to the release of Si, Mg and Ca from the mineral

344   bulk (**Table 1**). The amounts of released Si, Mg and Ca correspond to 2%, 4% and 17% of the

345   total content, respectively. On the contrary, release of Fe was not observed for any dissolution

346   time, likely due to the negligible solubility of iron in the adopted experimental conditions.

347   These results are in good agreement with those obtained via XPS on the fibre surface, where a

348   depletion of Si and Mg of treated fibres with respect to the untreated ones was observed

349   together with a significant increase of Fe content up to ca. 30% relative (**Table 2**). Possible

350   explanations for this latter increase are that, in the chosen experimental conditions, Fe is not

351   released and therefore accumulates on the fibre surface or, in alternative, it is mobilized from

352   the fibre surface but immediately precipitates from the solution. In the second hypothesis, part

353   of the $Fe(III)$ present in the oxidised external layer is supposed to have been mobilized and to

354   have immediately reacted with phosphate ions in the buffer solution, with consequent

355   precipitation on the fibre surface as iron phosphate, insoluble at neutral pH. This would lead

356   to an increase of iron phosphate with dissolution time paralleled by a decrease of $Fe(III)$

357   oxide-hydroxide, and is well supported by XPS results (**Fig. 5**).

358   Notably, the occurrence of iron phosphates together with remaining $Fe(III)$ oxide-hydroxides

359   on fibre surfaces is well in agreement with the Fe-bearing nanoparticles observed by TEM

360   and with P traces also observed in TEM-EDS analysis. The occurrence of new phases during

361   the leaching process, also described for other asbestos minerals (e.g., chrysotile asbestos,

362   Turci et al., 2007), accounts for the observed presence of iron-rich nanoparticles and is

363   relevant to modulate asbestos toxicity (Favero-Longo et al., 2009). An increase of surface Fe

364   concentration was already reported in Seal et al. (1996, 1997) for asbestos in contact with

365   both cell-bearing and cell-free biological media. Moreover, the precipitation of $Fe(III)$

366   phosphate was observed during the interaction between Fe oxyhydroxide and orthophosphate

367   ions (Lijklema, 1980), and the formation of FeOOH-orthophosphate surface complexes

368 during silicate dissolution in neutral aqueous solutions was evidenced by Schott et al. (1983).

369 According to Person et al. (1996), the direct bond between surface metal iron and phosphate

370 involves the formation of monodentate surface complexes. At pH 7.4 the most

371 thermodynamically stable Fe(III) phosphate complexes are -FePO$_4$H$^-$ and -FePO$_4$$^{2-}$. The

372 binding energy value of Fe-P signal observed in the present case (712.8 eV) is intermediate

373 between BE values of Fe(II)-P and Fe(III)-P (712.3 and 713.8eV, respectively) synthesised as

374 glasses and characterized by XPS and ToF-SIMS (Crobu, 2012). The presence of a mixture of

375 the two phosphates cannot be ruled out and the shift at higher BE might be also due to the

376 particle sizes that according to the TEM results are in the nanometer range. On the other hand

377 a possible contribution to Fe(II)–phosphate might also be due to the X-ray induced

378 degradation of the iron phosphate (Crobu, 2012).

379 In minerals as well as mineral nanoparticles, the dissolution process promotes the interaction

380 between bulk and surface, and this interaction may depend on particle size, morphology and

381 surface structure (Echigo et al. 2012). The untreated UICC crocidolite fibres have the bulk

382 enriched in Fe(II) with respect to the surface (Fe^{2+}/Fe$_{tot}$ ratios are 48% and 20%, respectively,

383 Fantauzzi et al., 2010). On this basis, it can be claimed that the dissolution process promotes

384 bulk Fe(II) sites to occur on the fibre surface. This is very relevant due to the recognised

385 primary role of Fe(II) in the ROS production (Pacella et al., 2012 and references therein). In

386 our experiments the dissolution of the fibres is particularly vigorous in the first hour (**Table**

387 **1**); the consequent promotion of Fe(II) sites on the fibre surface is maximum in the first hour

388 and is likely faster than oxidation rate, as revealed by the abrupt increases of Fe(II) content at

389 the surface (from ca. 20% to ca. 30% of the total Fe content, **Figure 5**). For longer dissolution

390 time the two processes likely approach equilibrium, as the Fe(II) content on the surface

391 remains almost constant and Fe(III) bonded to the silicate structure increases almost regularly

392 (**Figure 5**). The subsequent formation of Fe oxide-hydroxide and precipitation of Fe

393 phosphate may account for coating of the crocidolite fibres, which in turn may modulate

394 asbestos toxicity or eventually represents one of the mechanisms of formation of ferruginous

395 bodies, one of the key marker for the histopathological assessment of asbestosis in lung and

396 surrounding human tissues (Pascolo et al. 2013).

397 In addition to precipitation of Fe phosphate, the precipitation of Ca phosphate on fibre surface

398 may be invoked during dissolution of crocidolite, as suggested by combining the ICP and

399 XPS data. In fact, the rate of Ca release significantly decreases after 24-48 h (**Table 1**), and a

400 Ca2p$_{3/2}$ signal is measured starting from 24 h experiment (**Table 2**). The Ca-phosphate

401 precipitation was proved by Lu and Leng (2005) to occur at circa-neutral pH in simulated

402   body fluids containing 1.6-2.5 mmol*dm^{-3} (about 1/10 of the presently measured Ca amount).

403   According to thermodynamical data, at pH 7.4 octacalcium phosphate [OCP:

404    $Ca_8(HPO_4)_2(PO_4)_4*5H_2O$] and hydroxyapatite [HA: $Ca_{10}(OH)_2(PO_4)_6$] may precipitate from

405   simulated body fluids. The BE of calcium in our sample is in good agreement with BE of Ca

406   in both HA and OCP (Chuesuei et al., 1999). In spite of the highest nucleation rate of OCP

407   with respect to HA, it is interesting to note that the formation of HA as a secondary phase

408   from dissolution of chrysotile and brucite was already observed under simulated lung

409   conditions, without any assistance from cells (Taunton et al., 2010). In addition, ions such as

410   Fe^{3+}, Fe^{2+}, Mg^{2+}, Na^+ and K^+ may be incorporated in Ca deficient hydroxyapatites (Morrisey

411   et al., 2005), therefore the precipitation of HA in our conditions seems to be very likely.

412

413   **5. CONCLUSIONS**

414

415   In this study we have investigated by ICP-OES, XPS and HR-TEM the dissolution process

416   and progressive surface modifications of UICC crocidolite fibres after suspension in a

417   hydrogen peroxide solution buffered at pH 7.4 for 0.5 h, 1 h, 24 h, 48 h, 168 h (one week) and

418   1440 h (two months). The dissolution experiments were repeated with and without H_2O_2: after

419   the first hour results did not show marked differences. The dissolution process evidenced two

420   steps: 1) between zero and 48 h, representing the undersaturation conditions, favourable to

421   fibre solubility; 2) after 48h – and markedly after 168 h – representing the near-saturation

422   conditions, where element release is very low or below the detection limit. Both

423   undersaturated (initial) and close-to-saturation (steady state) dissolution rates were tentatively

424   retrieved. Congruent dissolution of Si and Mg are observed in a proportion roughly

425   corresponding to crocidolite stoichiometry (both bulk and surface), Ca is released in excess

426   (possibly due to a contaminant impurity) and later precipitates, and Fe seems to be not

427   released. Consequently, fibre surface chemistry is progressively enriched in Fe coming from

428   the bulk and oxidized, firstly in the form of Fe(III) silicate, then in the forms of Fe(III) oxide-

429   hydroxide and Fe phosphate. This latter is presumably a mix of Fe(III) and Fe(II) phosphates,

430   even if a contribution to Fe(II) might also be a consequence of Fe(III) reduction under X-rays.

431   A conceivable explanation is that bulk Fe(II) is oxidized to Fe(III) and then mobilized from

432   the fibre surface, but immediately precipitates after reaction with phosphate ions in the buffer

433   solution, with consequent precipitation on the fibre surface of a Fe phosphate, insoluble at

434   neutral pH. In fact, crocidolite structure, fibrous habit and high aspect ratio are indeed

435   preserved after dissolution, but a fibre coating enriched in Fe(III) oxide-hydroxide and Fe(III)

436 phosphate occurs and Fe-bearing nanoparticles are clearly visible on fibre surface after
437 dissolution. This is highly relevant, because the process of coating of the fibres with Fe-rich
438 phases is candidate to modulate asbestos toxicity and may eventually represent one of the
439 mechanisms of formation of ferruginous bodies.
440
441
442   **ACKNOWLEDGMENTS**
443

447
448   **APPENDIX A. SUPPLEMENTARY DATA**
449
450   **REFERENCES**
451

452 Avantage Software v. 3.45, Thermo Fisher Scientific Inc. – Micro Focus Ltd.

453 Bergamini C., Fato R., Biagini G., Pugnaloni A., Giantomassi F., Foresti E., Lesci G. I.,
454   Roveri N. and Lenaz G. (2007) Mitochondria changes induced by natural and synthetic
455   asbestos fibers: Studies on isolated mitochondria. *Cell. Mol. Biol.* **52 Suppl.**, OL 905-
456   913.

457 Chao C. C., Lund L. G., Zinn K. R. and Aust A. E. (1994) Iron mobilization from crocidolite
458   asbestos by human lung carcinoma cells. *Arch. Biochem. Biophys.* **314**, 384-391.

459 Chuesuei C. C., Goodman D. W., Van Stipdonk M. J., Justes D. R. and Schweikert E. A.
460   (1999) Calcium Phosphate Phase Identification Using XPS and Time–of–Flight Cluster
461   SIMS. *Anal. Chem.* **71**, 149-153.

462 Crobu M. (2012) Diss. ETH N° 20251.

463 Crobu M., Rossi A., Mangolini F. and Spencer N. D. (2010) Tribochemistry of bulk zinc
464   metaphosphate glasses. *Tribology Letters* **39**, 121-134.

465 Echigo T., Aruguete D. M., Murayama M. and Hochella M. F. (2012) Influence of size,
466   morphology, surface structure, and aggregation state on reductive dissolution of
467   hematite nanoparticles with ascorbic acid. *Geochim. Cosm. Acta* **90**, 149-162.

468 Fairley N. (1999-2003) CasaXPS Version 2.3.15

469 Fantauzzi M., Pacella A., Atzei D., Gianfagna A., Andreozzi G. B. and Rossi A. (2010)
470   Combined use of X-Ray Photoelectron and Mössbauer spectroscopic techniques in the
471   analytical characterization of iron oxidation state in amphibole asbestos. *Anal. Bioanal.*
472   *Chem.* **396**, 2889-2898.

473 Fantauzzi M., Pacella A., Fournier J., Gianfagna A., Andreozzi G. B. and Rossi A. (2012)
474   Surface chemistry and surface reactivity of fibrous amphibole that are not regulated as
475   asbestos. *Anal. Bioanal. Chem.* **404**, 821-833.

476 Favero-Longo S. E., Turci F., Tomatis M., Compagnoni R., Piervittori R. and Fubini B.
477   (2009) The Effect of Weathering on Ecopersistence, Reactivity, and Potential Toxicity
478   of Naturally Occurring Asbestos and Asbestiform Minerals. *J. Toxicol. Env. Heal. A*,
479   **72**, 305-314.

480 Fubini B. (1997) Surface reactivity in the pathogenic response to particulates. *Environ. Health*
481   *Persp.* **105**, 1013-1020.

482 Fubini B. and Otero-Arean C. (1999) Chemical aspects of the toxicity of inhaled mineral
483   dusts, *Chem. Soc. Rev.* **28**, 373-381.

484 Fubini B., Mollo L. and Giamello E. (1995) Free radical generation at the solid/liquid
485   interface in iron containing minerals. *Free Radic. Res.*, **23**, 593-614.

486 Fubini, B., Fenoglio, I., Tomatis, M., and Turci, F. (2011) Effect of chemical composition and
487   state of the surface on the toxic response to high aspect ratio nanomaterials (HARNS)
488   *Nanomedicine* **6**, 899-920.

489 Gold J., Amandusson H., Krozer A., Kasemo B., Ericsson T., Zanetti G. and Fubini B. (1997)
490   Chemical characterization and reactivity of Iron Chelator-treated Amphibole Asbestos,
491   *Environ. Health Persp.* **105**, 1021-1030.

492 Gries W.H. (1996) A Universal Predictive Equation for the Inelastic Mean Free Pathlengths
493   of X-ray Photoelectrons and Auger Electrons. *Surf. Interface Anal.* **24**, 38-50.

494 Gronow J.R. (1987) The dissolution of asbestos fibres in water. *Clay Miner.* **22**, 21-35.

495 Gunter M.E., Belluso E. and Mottana A. (2007) Amphiboles: Environmental and Health
496   Concerns. *Rev. Mineral. Geochem.* **67**, 453-516.

497 Hardy J. A. and Aust A. E. (1995) Iron in asbestos chemistry and carcinogenicity. *Chem. Rev.*
498   **118**, 95-97.

499 Hochella M. F. (1993) Health Effects of Mineral Dust. *Rev. Mineral. Geochem.* **28**, 275-308.

500 Hohr D., Steinfartz Y., Schins R. P., Knaapen A. M., Martra G., Fubini B. and Borm P. J.
501   (2002) The surface area rather than the surface coating determines the acute
502   inflammatory response after instillation of fine and ultrafine TiO2 in the rat. *Int. J. Hyg.*
503   *Envir. Heal.* **205**, 239-244

504 Hume L. A. and Rimstidt J. D. (1992) The biodurability of chrysotile asbestos. *Amer. Min.***77**,
505   1125-1128.

506 Kamp D. W. and Weitzman S. A. (1999) The molecular basis of asbestos induced lung injury.
507   *Thorax* **54**, 638-652.

508 Landis W. J. and Martin J. R. (1984) X-ray photoelectron spectroscopy applied to gold-
509   decorated mineral standards of biological interest. *J. Vac. Sci. Technol. A***2**, 1108-1111.

510 Lijklema L. (1980) Interaction of Orthophosphate with Iron (III) and Aluminum Hydroxides,
511   *Environ. Sci. Technol.* **14**, 537-541.

512 Liu G., Cheresh P. and Kamp D. W. (2013) Molecular basis of asbestos-induced lung disease.
513   *Annu. Rev. Pathol.* **8**, 161-187.

514 Lu X. and Leng Y. (2005) Theoretical analysis of calcium phosphate precipitation in
515   simulated body fluid. *Biomaterials* **26**, 1097-1108.

516 Lund L. G. and Aust A. E. (1992) Iron mobilization from crocidolite asbestos greatly enhances
517   crocidolite-dependent formation of DNA single-strand breaks in øX174 RFI DNA.
518   *Carcinogenesis* **13**, 637-642.

519 Martra G., Tomatis M., Fenoglio I., Coluccia C. and Fubini B. (2003) Acid Modifies the
520   Surface of Asbestos: Possible Implications in the Molecular Mechanisms of Toxicity.
521   *Chem. Res. Toxicol.* **16**, 328-335.

522   Morrisey R., Rodriguez-Lorenzo L. M. and Gross K. A. (2005) Influence of ferrous iron
523   incorporation on the structure of hydroxyapatite. *J. Mater. Sci.* **16**, 387-392.

524   Mura E. (2010) Master thesis "Polifosfati di calcio e di zinco: caratterizzazione chimica e
525   proprietà meccaniche" December 17, University of Cagliari and ETH Zurich.

526   Nejjari A., Fournier J., Pezerat H. and Leanderson P. (1993) Mineral fibres: correlation
527   between oxidising surface activity and DNA base hydroxylation. *Br. J. Ind. Med.* **50**,
528   501-504.

529   Oze C. and Solt K. (2010) Biodurability of chrysotile and tremolite asbestos in simulated lung
530   and gastric fluids. *Amer. Min.* **95**, 825-831.

531   Pacella A., Andreozzi G. B. and Fournier J. (2010) Detailed crystal chemistry and iron
532   topochemistry of asbestos occurring in its natural setting: a first step to understanding
533   its chemical reactivity. *Chem. Geol.* **277**, 197-206.

534   Pacella A., Andreozzi G. B., Fournier J., Stievano L., Giantomassi F., Lucarini G., Rippo M.
535   R. and Pugnaloni A. (2012) Iron topochemistry and surface reactivity of amphibole
536   asbestos: relations with in vitro toxicity. *Anal. Bioanal. Chem.* **402**, 871-881.

537   Pascolo L., Gianoncelli A., Schneider G., Salomé M., Schneider M., Calligaro C., Kiskinova
538   M., Melato M., and Rizzardi C. (2013) The interaction of asbestos and iron in lung
539   tissue revealed by synchrotron-based scanning X-ray microscopy. Nature Scientific
540   Reports **3**, 1123.

541   Person P., Nilsson N. and Sjoberg S. (1996) Structure and Bonding of Orthophosphate Ions at
542   the Iron Oxide-Aqueous Interface. *J. Colloid Interf. Sci.* **177**, 263-275.

543   Reilman R. F., Msezane A. and Manson S. T. J. (1976) Relative intensities in photoelectron
544   spectroscopy of atoms and molecules. *J. Electron. Spectrosc. Relat. Phenom.* **8**, 389-
545   394.

546   Rossi A., Piras F. M., Kim D., Gellman A. J. and Spencer N. D (2006) Surface reactivity of
547   tributylthiophosphate: Effects of temperature and mechanical stress. *Tribology Letters*,
548   **23**, 197-208.

549   Scofield J. H. (1976) Hartree-Slater subshell photoionization cross-sections at 1254 and 1487
550   eV. *J. Electron. Spectrosc.* **8**, 129-137

551 Schott J. and Berner R. A. (1983)   X-ray photoelectron studies of the mechanism of iron
552   silicate dissolution during weathering. *Geochim. Cosmochim. Acta* **47**, 2233-2240.

553 Seal S., Krezoski S., Barr T. L., Petering D. H., Klinowski J. and Evans P. H. (1996) Silicate
554   Surface Chemistry and Biological Pathogenicity: An X-ray Photoelectron Spectroscopic
555   Study. *Proc. R. Soc. Lond.* **263**, 943-951.

556 Seal S., Krezosky S., Barr T. L., Petering D. H., Klinowsky J. and Evans P. H. (1997) Surface
557   Chemical interaction of fibrous asbestos with biocells: an ESCA study. *J. Haz. Mater.*
558   **53**, 57-74.

559 Seah M. P. (2003) Quantification in AES and XPS. In: Briggs D, Grant JT (eds) Surface
560   Analysis by Auger and X-Ray Photoelectron Spectroscopy. IM Publication Surface
561   Science Spectra, Manchester.

562 Shen Z., Bosbach D., Hochella M. F. Jr, David L. B., Williams M. G. Jr., Dodson R. F. and
563   Aust, A. E. (2000) Using in Vitro Iron Deposition on Asbestos To Model Asbestos
564   Bodies Formed in Human Lung. *Chem. Res. Toxicol.* **13**, 913-921.

565 Shirley D. A. (1972) High resolution X-Ray photoemission spectrum of the valence bands of
566   gold. *Phys. Rev.* B**5**, 4709-4714.

567 Shukla A., Gulumian M., Hei T. K., Kamp D., Rahman Q. and Mossman B. T. (2003)
568   Multiple roles of oxidants in the pathogenesis of asbestos-induced diseases. *Free Radic.*
569   *Biol. Med.* **34**,1117-1129.

570 Stanton M. F., Layard M., Tegeris A., Miller E., May M., Morgan E. and Smith A. (1981)
571   Relation of particle dimension to carcinogenicity in amphibole asbestoses and other
572   fibrous minerals. *J. Nat. Cancer Inst.* **67**, 965-975.

573 Taunton A. E., Gunter M. E., Druschel G. K. and Wood S. A. (2010) Geochemistry in the
574   lung: Reaction-path modelling and experimental examination of rock forming minerals
575   under physiological conditions. *Amer. Min.* **95**, 1624-1635.

576 Turci F., Tomatis M., Lesci I. G., Roveri N. and Fubini B. (2011) The iron-related molecular
577   toxicity mechanism of synthetic asbestos nanofibres: a model study for high-aspect-
578   ratio nanoparticles. *Chemistry* **17**, 350-358.

579 Turci F., Favero-Longo S. E., Tomatis M., Martra G., Castelli D., Piervittori R. and Fubini B.
580   (2007) A Biomimetic Approach to the Chemical Inactivation of Chrysotile Fibres by
581   Lichen Metabolites. *Chem. Eur. J.* **13**, 4081-4093.

582 Werner J., Hochella M. F., Guthrie G. D., Hardy J. A., Aust A. E. and Rimstidt J. D. (1995)
583   Asbestiform riebeckite (crocidolite) dissolution in the presence of Fe chelators:
584   implications for mineral-induced disease. *Amer. Min.* **80**, 1093-1103.

585

586 **Captions to Figures**

587

588 Figure 1: FE-SEM images of untreated UICC crocidolite fibres at increasing magnification:
589 large, polygonal fibres as well as single fibrils (coming from partition of previous ones) are
590 evident.

591

592 Figure 2: Dissolution of UICC crocidolite fibres in phosphate buffered solution at pH 7.4 with
593 H_2O_2 in the range 0-1440 h: a) released Si; b) released Mg; c) released Ca (in this case the
594 interval 0-168 h was plot to better highlight the Ca precipitation after 48 h).

595

596 Figure 3: Dissolution of UICC crocidolite fibres in phosphate buffered solution at pH 7.4:
597 released Si and Ca vs. Mg. Data of solution with and without H_2O_2 are plot and no differences
598 are observed.

599

600 Figure 4: XPS high-resolution spectra after background subtraction and curve fitting of
601 Fe2p3/2 peak of UICC crocidolite fibres after 0.5, 1, 24, 48 and 168 h of incubation in
602 phosphate buffered solution at pH 7.4 with H_2O_2. Four components, Fe(II)–O (BE = 709.0 ±
603 0.2), Fe(III)–O (BE = 710.5 ± 0.2), Fe(III)–OOH (BE = 711.6 ± 0.2) and Fe–P (BE = 712.8 ±
604 0.2), have been resolved.

605

606 Figure 5: Quantitative evolution of the $Fe2p_{3/2}$ components (in % of $Fe2p_{3/2}$ total peak area)
607 detected on the surface of the UICC crocidolite fibres after 0.5, 1, 24, 48 and 168 h of
608 incubation in phosphate buffered solution at pH 7.4 with H_2O_2.

609

610 Figure 6: Representative TEM images of untreated UICC crocidolite fibre taken at increasing
611 magnification. Fibre bundles and single asbestos fibrils are clearly visible in the low-to-
612 medium magnification images (A, B and C). HR-TEM image (D) displays the highly ordered
613 crystal lattice of the pristine fibre.

614

615 Figure 7: Representative TEM images of a UICC crocidolite fibre leached in phosphate
616 buffered solution at pH 7.4 with H_2O_2 for 168 h. Fibre bundles and single asbestos fibrils are
617 clearly visible in the low-magnification image (A). At higher magnification (B, C and D) the
618 occurrence of a neo-formed nanoparticle is observed (white arrows). Though crocidolite

619   crystal lattice is preserved after dissolution (D), some possibly amorphous nanoparticle are
620   visible on top of the asbestos fibre.

621

622   Figure A.1: XP-survey spectra.

623

624   Figure A.2: Surface composition obtained on fibres suspended in the solution with and
625   without H_2O_2.

626

627   Figure A.3: $Fe2p_{3/2}$ components (in % of $Fe2p_{3/2}$ total peak area) obtained on fibres suspended
628   in the solution with and without H_2O_2.

Table 1. Results of ICP-OES analyses of UICC Crocidolite fibres after incubation in phosphate buffered solution at pH 7.4 with and without H_2O_2 for 0.5, 1, 24, 48, 168 and 1440 h. Standard deviations (in brackets) were calculated over three measurements

Incubation time (h)	Incubation with H_2O_2			Incubation without H_2O_2		
	Mg (mg/kg)	Ca (mg/kg)	Si (mg/kg)	Mg (mg/kg)	Ca (mg/kg)	Si (mg/kg)
0.5	180(24)	877(67)	624(79)	-	-	-
1	224(17)	1082(46)	1110(107)	184	775	467
24	370(19)	1508(122)	3011(176)	331	1384	2977
48	460(8)	1531(121)	3772(37)	403	1470	3417
168	503(43)	1239(141)	4087(327)	447	1398	4066
1440	590(7)	866(25)	5120(72)	-	-	-

Table 2: Surface analysis of UICC crocidolite fibres by XPS before (t = 0 h) and after dissolution in phosphate buffered solution at pH 7.4 with H_2O_2 for 0.5, 1, 24, 48 and 168 h: atomic percentages of elements (at. %) for the various incubation times. In the lowest part of the Table the surface composition is recalculated considering only Si, Mg, Ca and Fe. Standard deviations (in brackets) were calculated over three measurements

Dissolution time (h)	Composition (at. %)							
	Fe	O	Si	Na	Mg	Ca	P	K
0	5.2 (0.5)	64 (3)	23 (1)	3.3 (0.3)	3.8 (0.4)	--	--	--
0.5	4.9 (0.3)	62 (1)	23 (1)	2.8 (0.2)	2.2 (0.4)	--	3.1 (0.1)	1.3 (0.1)
1	4.8 (0.2)	59.3 (0.3)	21.5 (0.2)	3.3 (0.1)	2.0 (0.2)	--	4.0 (0.4)	5.1 (0.4)
24	5.6 (0.1)	60.8 (0.5)	20 (1)	3.3 (0.1)	2.5 (0.1)	1.11 (0.04)	5.8 (0.3)	1.1 (0.2)
48	5.6 (0.1)	61.7 (0.1)	19.4 (0.1)	3.1 (0.1)	2.4 (0.1)	1.1 (0.1)	5.5 (0.1)	1.1 (0.1)
168	5.7 (0.1)	61.1 (0.1)	18 (1)	2.9 (0.2)	2.4 (0.4)	1.4 (0.8)	7.0 (0.2)	1.1 (0.3)

Dissolution time (h)	Composition: Fe – Si – Ca – Mg (at. %)			
	Fe	Si	Mg	Ca
0	16 (1)	72 (3)	12 (1)	--
0.5	16 (1)	77 (2)	7 (1)	
1	17.0 (0.5)	76 (1)	7.0 (0.5)	-
24	19.4 (0.3)	68.2 (0.3)	8.5 (0.1)	3.9 (0.2)
48	19.4 (0.4)	68.1 (0.4)	8.3 (0.2)	4.0 (0.3)
168	21 (1)	65.7 (0.4)	8.7 (0.4)	5 (1)

Data for t = 0 h and for bulk composition of UICC crocidolite (Na 4.1; Si 20.7; O 61.5; Fe 10.7; Mg 2.2; Al 0.1; Ca 0.7 at. %) are from Fantauzzi et al. (2010).

Table 3: Mean binding energy values of the most intense XPS signals of UICC crocidolite before (t = 0 h) and after dissolution in phosphate buffered solution at pH 7.4 with H_2O_2 for 0.5, 1, 24, 48 and 168 h. Standard deviations (in brackets) were calculated over three measurements

Dissolution time (h)	Binding Energy (eV)									
	Si2p	Mg2p	Ca2p$_{3/2}$	Na1s	P2p$_{3/2}$	K2p$_{3/2}$	Fe2p$_{3/2}$ Fe(II)-O	Fe2p$_{3/2}$ Fe(III)-O	Fe2p$_{3/2}$ Fe(III)-OOH	Fe2p$_{3/2}$ Fe-P
0	102.4 (0.2)	49.4 (0.2)	--	1072.4 (0.2)	--	--	709.0 (0.2)	710.5 (0.2)	711.6 (0.2)	--
0.5	102.4 (0.2)	49.6 (0.2)	--	1072.4 (0.2)	134.0 (0.2)	293.2 (0.1)	709.2 (0.2)	710.7 (0.2)	711.8 (0.2)	712.8 (0.2)
1	102.3 (0.2)	49.6 (0.2)	--	1072.2 (0.2)	133.9 (0.1)	293.0 (0.1)	709.2 (0.2)	710.6 (0.2)	711.8 (0.2)	712.8 (0.2)
24	102.5 (0.2)	49.5 (0.2)	347.8 (0.2)	1072.3 (0.2)	133.7 (0.1)	293.3 (0.1)	709.0 (0.2)	710.6 (0.2)	711.6 (0.2)	712.7 (0.2)
48	102.4 (0.2)	49.46 (0.2)	347.9 (0.2)	1072.3 (0.2)	134.0 (0.2)	293.3 (0.1)	709.0 (0.2)	710.5 (0.2)	711.7 (0.2)	712.8 (0.2)
168	102.6 (0.2)	49.5 (0.2)	347.8 (0.2)	1072.2 (0.2)	133.8 (0.1)	293.2 (0.1)	709.1 (0.2)	710.5 (0.2)	711.6 (0.2)	713.0 (0.2)

Data for t = 0 h are from Fantauzzi et al. (2010)

Table 4. HR-TEM data of UICC crocidolite before and after dissolution in phosphate buffered solution at pH 7.4 with H_2O_2 for 168 h: calculated diffraction fringes distance and crystallographic planes assigned from Joint Committee on Powder Diffraction Standards (JCPDS) reference no. 19-1061

d exp (Å)	d ref (Å) 19-1061	Δ	*hkl* plane
UICC Crocidolite, untreated			
4.489	4.510	-0.02	0 4 0
4.876	4.890	-0.01	-1 1 1
UICC Crocidolite, treated			
2.545	2.541	0.00	-2 6 0
2.591	2.602	-0.01	0 6 1
3.250	3.270	-0.02	-2 4 0
4.913	4.890	0.02	-1 1 1

Figure 1
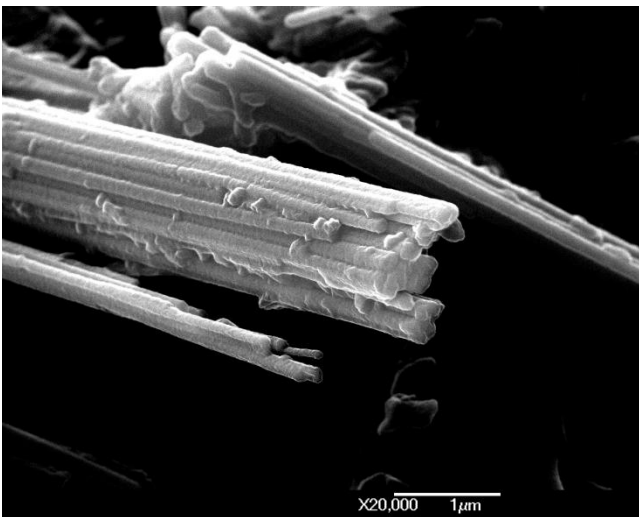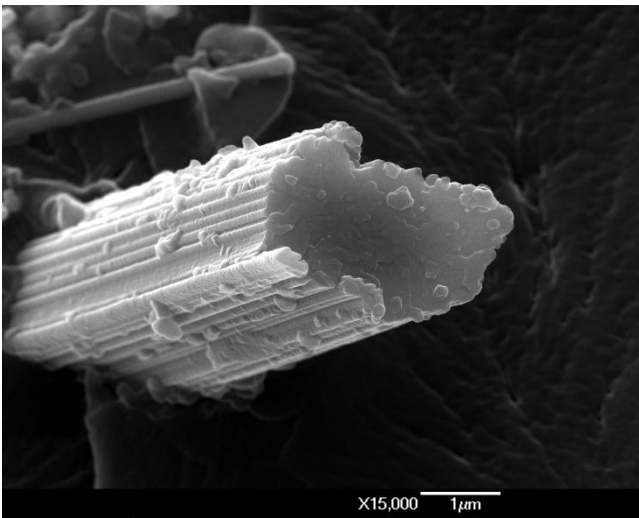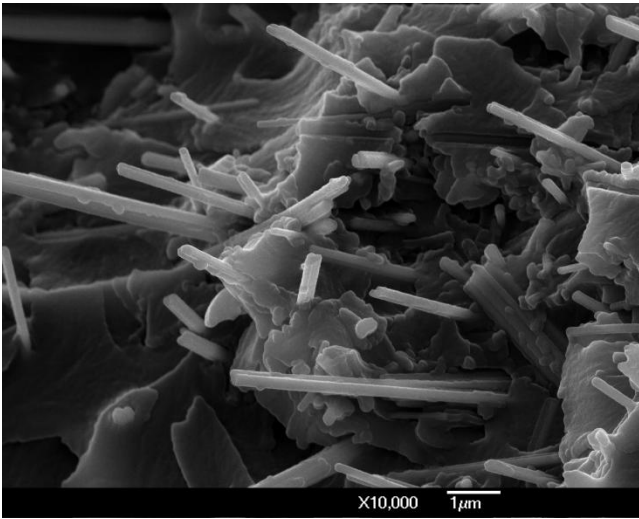
Figure 1

Figure 2
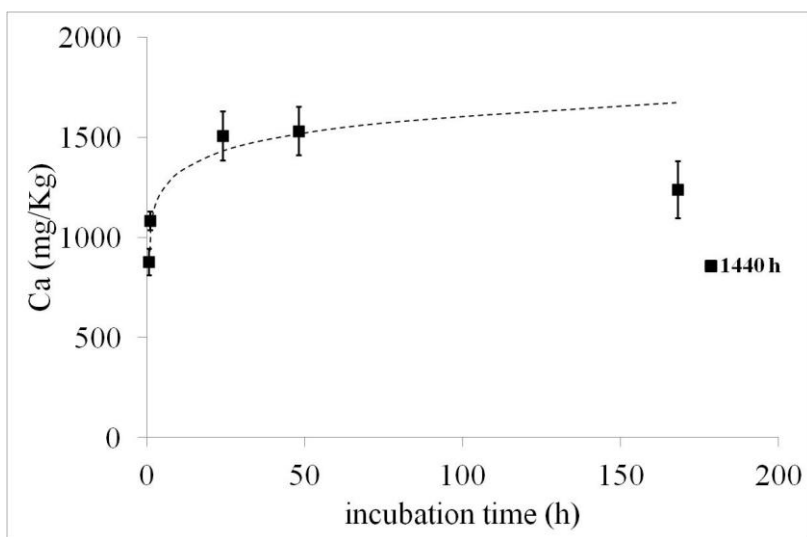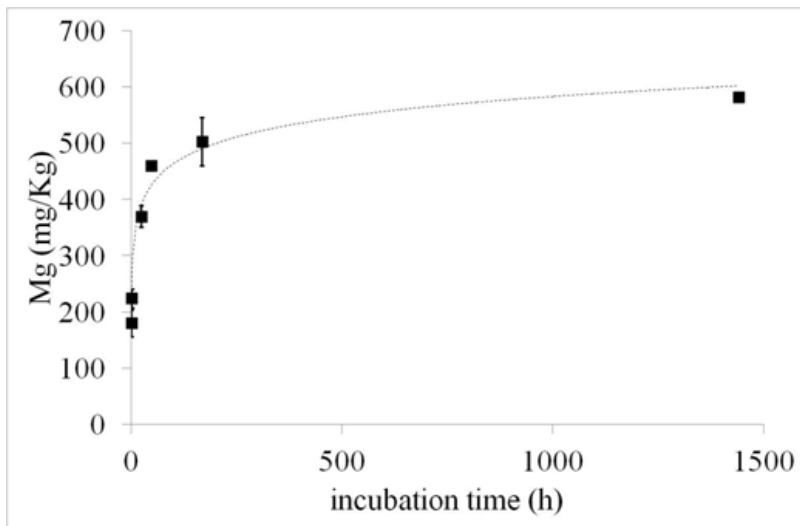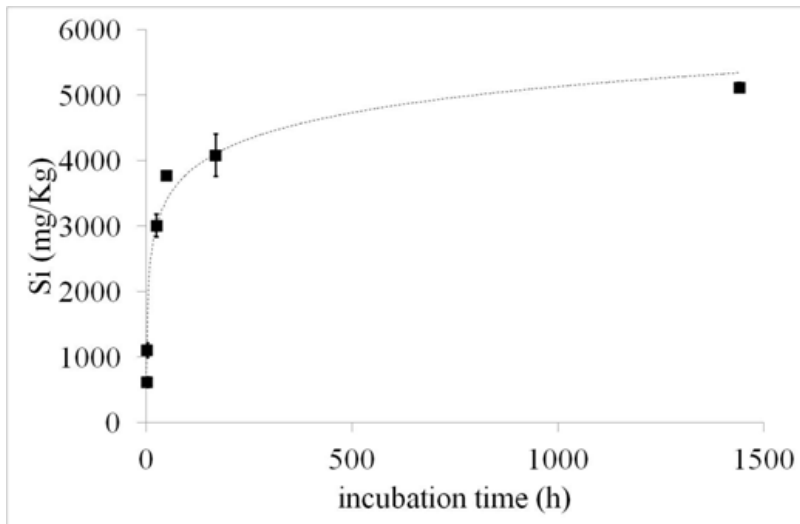
Figure 2

Figure 3
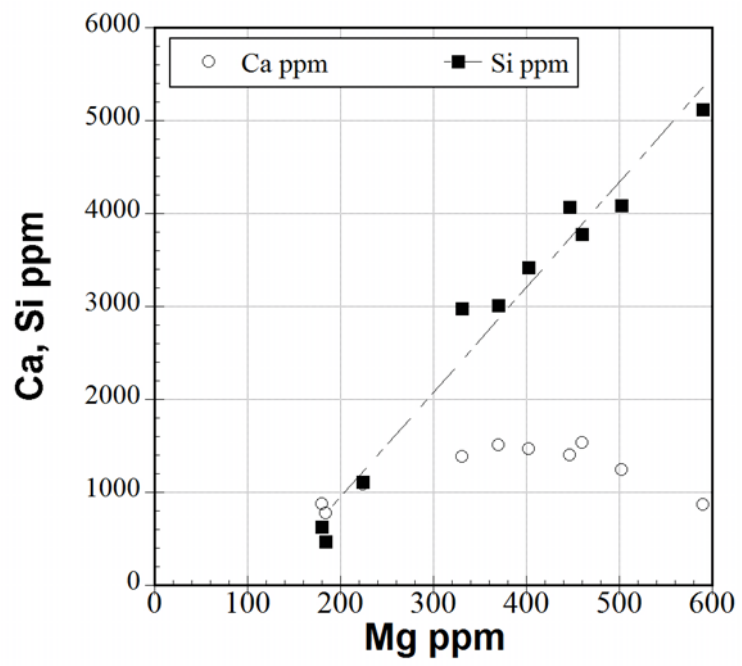
Figure 3

Figure 4
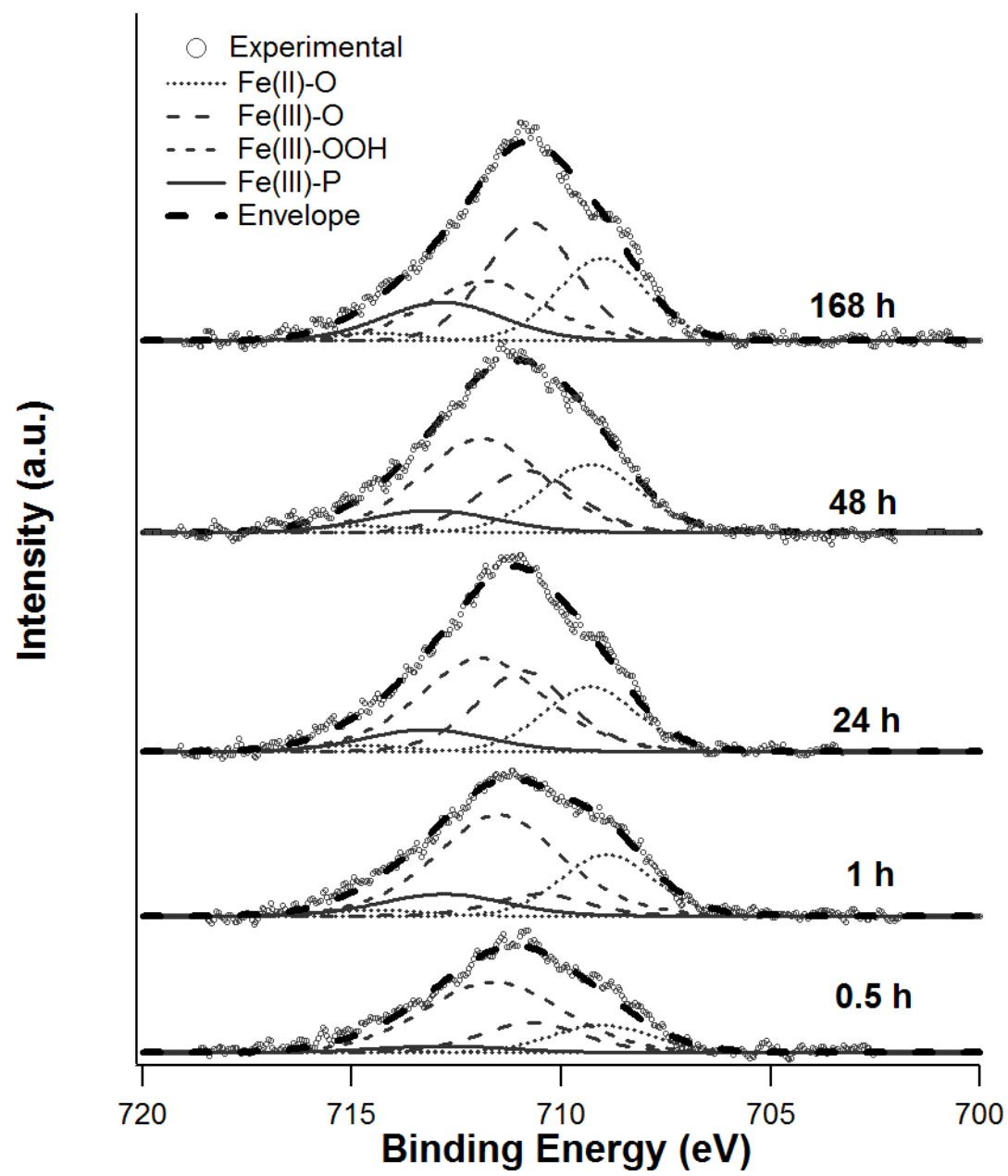
Figure 4

Figure 5
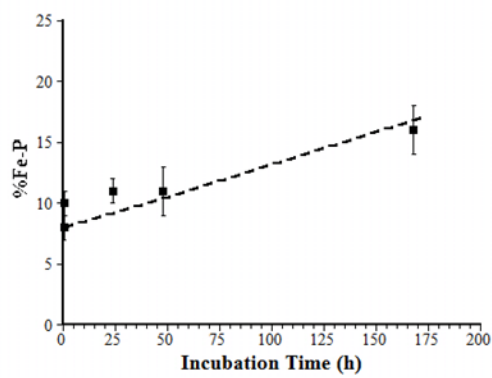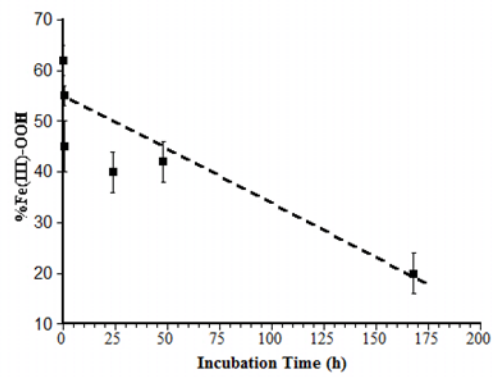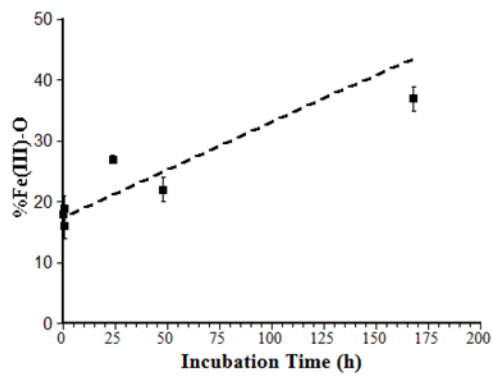
Figure 5

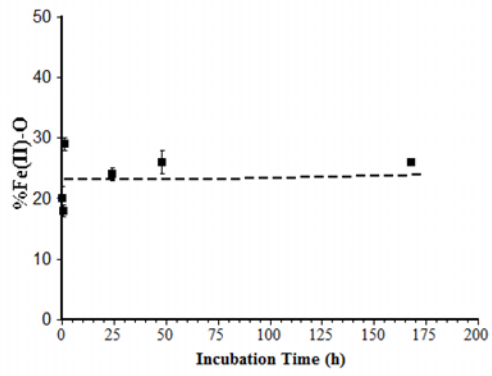**Figure 6**

Figure 6

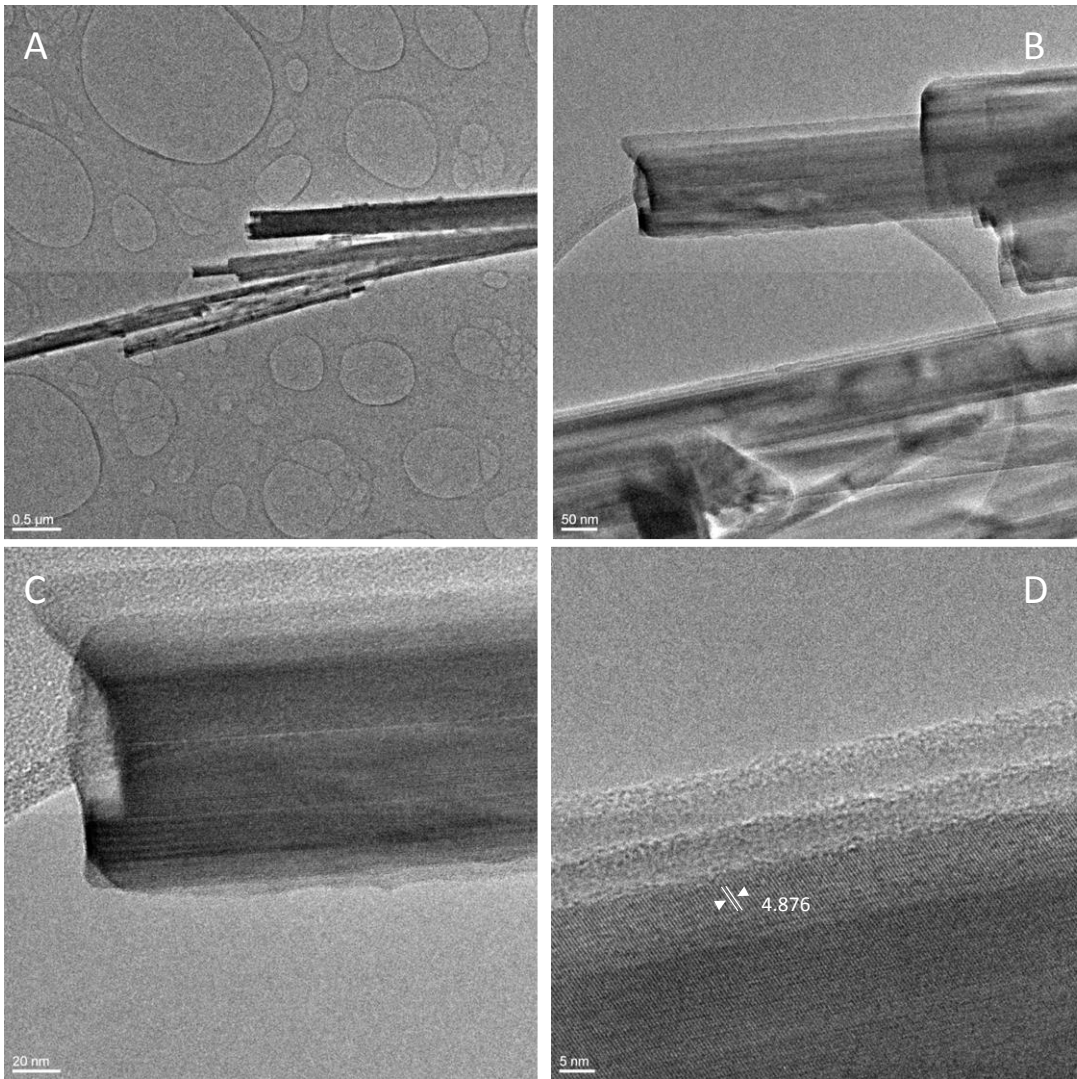**Figure 7**
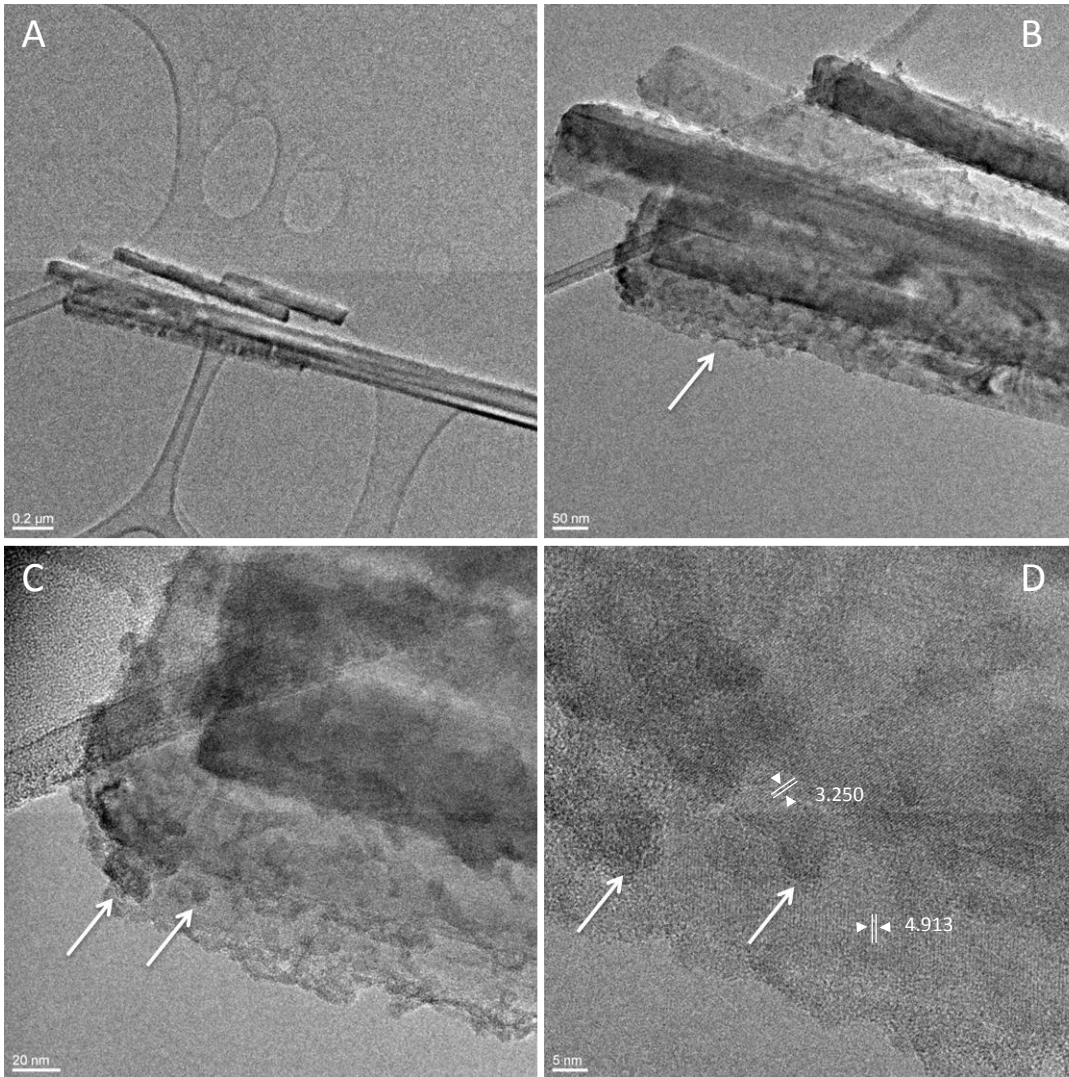
Figure 7

Figure A.1

Figure A.2

Click here to download Electronic Annex: Figure A.2.JPG

Figure A.3